

# Motion-Enhanced Nonlocal Similarity Implicit Neural Representation for Infrared Dim and Small Target Detection

Pei Liu, Yisi Luo<sup>\*</sup>, Wenzhen Wang, Xiangyong Cao<sup>\*</sup>  
Xi'an Jiaotong University  
Xi'an 710000, China

## Abstract

Infrared dim and small target detection presents a significant challenge due to dynamic multi-frame scenarios and weak target signatures in the infrared modality. Traditional low-rank plus sparse models often fail to capture dynamic backgrounds and global spatial-temporal correlations, which results in background leakage or target loss. In this paper, we propose a novel motion-enhanced nonlocal similarity implicit neural representation (INR) framework to address these challenges. We first integrate motion estimation via optical flow to capture subtle target movements, and propose multi-frame fusion to enhance motion saliency. Second, we leverage nonlocal similarity to construct patch tensors with strong low-rank properties, and propose an innovative tensor decomposition-based INR model to represent the nonlocal patch tensor, effectively encoding both the nonlocal low-rankness and spatial-temporal correlations of background through continuous neural representations. An alternating direction method of multipliers is developed for the nonlocal INR model, which enjoys theoretical fixed-point convergence. Experimental results show that our approach robustly separates dim targets from complex infrared backgrounds, outperforming state-of-the-art methods in detection accuracy and robustness.

## Keywords

Infrared Images, Implicit Neural Representation, Nonlocal Similarity, Motion Estimation, Dim and Small Target Detection

## 1 Introduction

Infrared dim and small target detection (IDSTD) is widely used in target warning, maritime rescue, and long-range search [33, 37, 39], etc. The small target size ( $2 \times 2$  to  $9 \times 9$  pixels) leads to weak features and indistinct texture, while complex, variable backgrounds introduce noise and clutter, making IDSTD a challenging task.

There are two main approaches to addressing the IDSTD problem: model-based methods and data-driven methods. Model-based methods [4, 9, 12, 34, 48] use domain knowledge to iteratively solve the objective function for target-background separation. These methods are interpretable and independent of data volume and labels but have limited representational capacity for complex scenes. Data-driven methods [8, 18, 38, 44, 45], using complex networks, generally outperform traditional methods, but depend on labeled data and struggle with out-of-distribution data.

Recently, implicit neural representations (INR) [28, 31] have emerged as a powerful paradigm for unsupervised tensor data representation. INR uses a multilayer perceptron (MLP) to learn a function that maps discrete coordinate tensors to continuous space, modeling complex data structures and showing strong performance in various tasks [28, 29, 31]. However, classical INR approaches lack domain knowledge. Luo et al. [27] addressed this by introducing

a low-rank constrained INR, incorporating prior knowledge to regularize images and improve background recovery. However, it overlooks sparse target and focuses on static images, lacking temporal representation. Inspired by these pioneer works, we propose a nonlocal low-rank INR method for IDSTD, incorporating nonlocal similarity and dynamic multi-frame background representation through motion estimation to improve target separation.

To combine the strengths of model-based and data-driven approaches, we propose a motion-enhanced nonlocal similarity INR model (optNL-INR) for IDSTD. Using motion information between consecutive frames, we compute the motion intensity of targets via optical flow, improving target location estimation and reducing target loss. Moreover, our method constructs a spatial-temporal tensor (STT) model by acquiring nonlocal similar patches and approximating background patches using low-rank INR within the continuous domain, capturing nonlocal low-rankness and global spatial-temporal correlations of the multi-frame background. This enables more accurate background estimation and target separation. Finally, we use 3D total variation (3DTV) and alternating direction method of multipliers (ADMM) to capture local smoothness and ensure stable optimization. The proposed motion-enhanced nonlocal INR method for IDSTD is unsupervised and does not rely on labeled data. The contributions of this work include:

- We propose the unsupervised optNL-INR method for IDSTD. We first introduce a multi-frame optical flow fusion strategy to estimate subtle target motion, enabling robust motion saliency estimation that strengthens target localization and effectively addresses target loss.
- We propose a novel nonlocal INR model with tensor Tucker decomposition to represent the infrared background tensor, which effectively captures both the nonlocal low-rankness and global spatial-temporal correlations of infrared backgrounds, largely improving small target detection.
- We provide theoretical guarantees for the existence of the nonlocal INR model, the spatial-temporal correlation bound brought by the smoothness of INR, and the fixed-point convergence of the ADMM algorithm, ensuring solid theoretical foundations and reliability of our method for IDSTD.
- Extensive experiments on infrared multi-frame datasets demonstrate the superior performance of our motion enhanced nonlocal INR method in detecting dim and small targets in infrared images against state-of-the-art baselines.

## 2 Related Work

### 2.1 Single-Frame-Based Methods

In recent years, significant progress has been made in single-frame IDSTD methods. The model-based methods initially evolved from

classical background suppression filtering techniques [9, 30]. Subsequently, the human visual system (HVS) [4, 24] and low-rank sparse decomposition (LRSD) were introduced. Notably, the introduction of the infrared patch image (IPI) model [12] based on LRSD method has inspired a series of developed work [42, 47, 48]. Subsequently, Dai et al. [6] introduced the reweighted infrared patch tensor (RIPT) model, enhancing the representation of data structures. Kong et al. [17] proposed a novel infrared small target detection method using nonconvex tensor fibered rank approximation (NTFRA), while Zhang et al. [48] introduced a robust approach utilizing the partial sum of the tensor nuclear norm (PSTNN), both of which significantly enhance detection performance in complex scenes.

Furthermore, data-driven deep methods have achieved significant performance improvements due to their powerful learning capabilities. Various deep learning (DL)-based techniques have been proposed, such as [18, 32, 39], which employ attention mechanisms to enable the model to focus on the most relevant features. The works presented in [19, 38, 50] utilize U-Net architectures to capture multi-scale features through their encoder-decoder structures. In contrast, the approaches in [2, 40, 46] adopt feature pyramid networks (FPNs) to exploit hierarchical multi-scale representations at different levels of granularity. Additionally, the methods proposed in [1, 8, 20] focus on contrast-based techniques, which highlight the distinctions between small targets and their backgrounds.

## 2.2 Multiple-Frame-Based Methods

Due to the limited availability of spatial information, spatial-temporal tensor (STT) models have been proposed. To enhance background estimation accuracy in complex scenes, Liu et al. [23] proposed a nonconvex tensor low-rank approximation (NTLA) method by adaptively assigning weights to singular values. Luo et al. [25] proposed the improved multi-mode nuclear norm joint local weighted entropy contrast (IMNN-LWEC) method, utilizing spatial-temporal tensor decomposition and adaptive regularization. Liu et al. [22] proposed a method that employs nonconvex tensor Tucker decomposition with factor priors (NFTDGSTV). To reduce redundant information, Wang et al. [34] developed a non-overlapping patch spatial-temporal tensor (NPSTT) model with tensor capped nuclear norm solving. To enhance the detection accuracy, Luo et al. [26] proposed a clustering and tracking-guided spatial-temporal prediction completion (CTSTC) model in the high-frequency domain.

In addition, data-driven multi-frame methods also effectively leverage spatiotemporal information. To enhance moving target detection, Zhang et al. [49] integrated an untrained 3D spatial-temporal prior module (3DSTPM) with convolution-based tensor nuclear norm and nested total variation regularization. Huang et al. [14] proposed the local motion-aware transformer (LMAFormer) by integrating a local motion-aware spatiotemporal attention mechanism and a multiscale fusion transformer. Chen et al. [5] introduced two dense moving infrared small target datasets, DMIST-60 and DMIST-100, and proposed the linking-aware sliced network (LAS-Net) as a baseline to enhance detection performance in dense target scenarios. Li et al. [19] introduced the direction-coded temporal U-shape module (DTUM), which enhances multi-frame infrared small target detection by encoding motion direction into features.

Although these data-driven methods have achieved performance improvements, their applications remain limited in cross-scene or few-shot tasks due to the supervised training with large labeled datasets. The black-box structure of these models results in a lack of interpretability. As compared, the proposed motion-enhanced nonlocal INR method optNL-INR is unsupervised, generalizable across different scenes, and enjoys better interpretability.

## 3 Methodology of OptNL-INR

### 3.1 Notations

The scalar, vector, matrix, and tensor are denoted as  $x$ ,  $\mathbf{x}$ ,  $\mathbf{X}$ , and  $\mathcal{X}$ , respectively. Given a tensor  $\mathcal{X} \in \mathbb{R}^{n_1 \times n_2 \times n_3}$ , the element at position  $(i, j, k)$  in  $\mathcal{X}$  is denoted as  $\mathcal{X}(i, j, k)$ . The Frobenius norm of a tensor  $\mathcal{X} \in \mathbb{R}^{n_1 \times n_2 \times n_3}$  is defined as  $\|\mathcal{X}\|_F = \sqrt{\sum_{i,j,k} \mathcal{X}(i, j, k)^2}$ . The mode- $i$  ( $i = 1, 2, 3$ ) unfolding operator of a tensor  $\mathcal{X} \in \mathbb{R}^{n_1 \times n_2 \times n_3}$  results in a matrix denoted by  $\text{unfold}_i(\mathcal{X}) = \mathbf{X}_{(i)} \in \mathbb{R}^{n_i \times \prod_{j \neq i} n_j}$ . The operator  $\text{fold}_i(\cdot)$  is defined as the inverse of  $\text{unfold}_i(\cdot)$ . The mode- $i$  product between a tensor  $\mathcal{X} \in \mathbb{R}^{n_1 \times n_2 \times n_3}$  with a matrix  $\mathbf{A} \in \mathbb{R}^{n \times n_i}$  is defined as  $\mathcal{X} \times_i \mathbf{A} = \text{fold}_i(\mathbf{A} \mathbf{X}_{(i)})$ .

*Definition 3.1 (Tensor Tucker rank [16]).* The Tucker rank of a tensor  $\mathcal{X} \in \mathbb{R}^{n_1 \times n_2 \times \dots \times n_N}$  is defined as

$$\text{rank}_T(\mathcal{X}) = \left( \text{rank}(\mathbf{X}_{(1)}), \text{rank}(\mathbf{X}_{(2)}), \dots, \text{rank}(\mathbf{X}_{(N)}) \right).$$

*Definition 3.2 (Tensor Tucker decomposition [16]).* For a tensor  $\mathcal{X} \in \mathbb{R}^{n_1 \times n_2 \times \dots \times n_N}$  with Tucker rank  $\text{rank}_T(\mathcal{X}) = (r_1, \dots, r_N)$ , there exist a core tensor  $\mathcal{C} \in \mathbb{R}^{r_1 \times \dots \times r_N}$  and  $N$  factor matrices  $\mathbf{U}_1 \in \mathbb{R}^{n_1 \times r_1}, \dots, \mathbf{U}_N \in \mathbb{R}^{n_N \times r_N}$  such that  $\mathcal{X}$  can be represented by  $\mathcal{X} = \mathcal{C} \times_1 \mathbf{U}_1 \times_2 \dots \times_N \mathbf{U}_N$ .

### 3.2 A General Model for IDSTD

Optimization-based approaches leverage the intrinsic low-rank structure of background components and the sparse distribution of targets under the robust principal component analysis (RPCA) framework [6] to represent STT, which can be expressed as follows:

$$\mathcal{D} = \mathcal{B} + \mathcal{T} + \mathcal{N}, \quad (1)$$

where  $\mathcal{D} \in \mathbb{R}^{n_1 \times n_2 \times n_3}$  is constructed by the input infrared image sequences  $\mathbf{I}_1, \mathbf{I}_2, \dots, \mathbf{I}_{n_3} \in \mathbb{R}^{n_1 \times n_2}$ .  $\mathcal{B}, \mathcal{T}, \mathcal{N} \in \mathbb{R}^{n_1 \times n_2 \times n_3}$  are the background tensor, target tensor, and noise tensor, respectively.

The overall flowchart of our proposed optNL-INR model for IDSTD is shown in Figure 2.

### 3.3 Motion Estimation for Infrared Images

Leveraging the inherent characteristics of infrared small target imagery and the assumption of brightness consistency for corresponding pixels in continuous scenes, the Farneback optical flow method [11] is employed to capture subtle motion, which determines the motion intensity and direction of moving targets. Our goal is to extract motion information in multi-frame images. The main steps of motion estimation are outlined below.

**Step 1.** Construct motion vector field tensor of pixel points. Given a pair of input images from adjacent frames,  $\mathbf{I}_1, \mathbf{I}_2 \in \mathbb{R}^{n_1 \times n_2}$ , we apply the proposed Farneback method to calculate the motion vector for each coordinate point. This results in the vector field matrices  $\mathbf{d}_x \in$

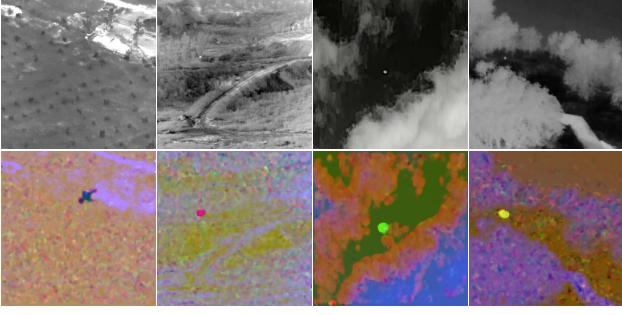


**Figure 1: Optical flow diagrams estimated for multiple infrared image scenes. The two-channel color images represent the intensities of motion vectors ( $\mathbf{d}_x, \mathbf{d}_y$ ).**

$\mathbb{R}^{n_1 \times n_2}$  and  $\mathbf{d}_y \in \mathbb{R}^{n_1 \times n_2}$ , which represent the motion direction and intensity of all pixel points in the horizontal and vertical directions, respectively. The matrices  $\mathbf{d}_x$  and  $\mathbf{d}_y$  are then combined into the motion vector field tensor  $\mathbf{v} = [\mathbf{d}_x, \mathbf{d}_y] \in \mathbb{R}^{n_1 \times n_2 \times 2}$ .

**Step 2.** Calculate the optical flow map. The actual motion direction and intensity of the pixel points are determined by the separated motion direction and intensity in the horizontal and vertical directions, and the optical flow maps for each frame  $f = 1, 2, \dots, n_3$  can be obtained as  $\mathbf{M}_f = \sqrt{|\mathbf{d}_x|^2 + |\mathbf{d}_y|^2}$ .

**Step 3.** Multi-frame fusion strategy. To enhance the robustness of motion estimation and mitigate transient outliers, we proposed a multi-frame optical flow fusion strategy. This strategy leverages the temporal consistency of targets across consecutive frames to aggregate optical flows from both the current frame and the previous  $k$  frames. The fused optical flow guides the detection of candidate targets and effectively addresses the target loss problem. The multi-frame fusion model is formulated by  $\mathbf{M}_f^F = \frac{1}{k+1} \sum_{i=0}^k \mathbf{M}_{f-i}$  and then stack the results

$$\mathcal{M}^F = \text{stack} \left( \mathbf{M}_1^F, \dots, \mathbf{M}_f^F, \dots, \mathbf{M}_{n_3}^F \right), \quad (2)$$

where  $\mathbf{M}_f^F \in \mathbb{R}^{n_1 \times n_2}$  denotes the fused optical flow map at the frame  $f$ ,  $k$  represents the number of previous frames, and  $\mathcal{M}^F \in \mathbb{R}^{n_1 \times n_2 \times n_3}$  is fused optical flow tensor map.

**Step 4.** Build the motion enhancement model. The weight map  $\mathcal{M}^F$  exhibits higher magnitudes in regions with salient motion targets. By performing weighted fusion with the original image  $\mathcal{D}$ , the response intensity of target regions is adaptively enhanced, thereby improving the detection accuracy and robustness. Specifically, the motion saliency features of moving targets are enhanced through spatial modulation using a weight map, while background noise interference is suppressed. The motion enhancement model is formulated by

$$\mathcal{X} = (1 - \gamma) \mathcal{D} + \gamma \mathcal{M}^F, \quad (3)$$

where  $\mathcal{D}$  is the original tensor in (1),  $\mathcal{X}$  is the motion-enhanced tensor, and  $\gamma$  is the balancing factor.

### 3.4 Nonlocal Grouping for STT

The background of infrared images usually exhibits strong *non-local* low-rankness. To capture this property, we conduct patch tensor splitting on the motion-enhanced tensor  $\mathcal{X} \in \mathbb{R}^{n_1 \times n_2 \times n_3}$  to obtain a series of small basic patch tensors  $\mathcal{P} \in \mathbb{R}^{p \times p \times n_3}$  in a

non-overlapping manner. Specifically, we slide a three-dimensional window over  $\mathcal{X}$  from left to right and top to bottom. The size of the window is  $p \times p$ , and the depth is  $n_3$ . To avoid redundancy, the sliding step is equal to  $p$ . Thus, we can obtain  $L = (n_1/p)(n_2/p)$  basic patch tensors to compose a basic patch tensors set  $\{\mathcal{P}_l \in \mathbb{R}^{p \times p \times n_3}\}_{l=1}^L$ . We conduct the same splitting for the coarse background  $\mathcal{X}'$  to obtain patches  $\{\mathcal{P}'_l \in \mathbb{R}^{p \times p \times n_3}\}_{l=1}^L$ , where  $\mathcal{X}'$  is obtained by leveraging the low-rank tensor function representation (LRTFR) [28]. This is achieved by optimizing the following model:

$$\begin{aligned} \min_{C, \theta_1, \theta_2, \theta_3} \sum_{(i,j,k)} |f_{\Theta}(i, j, k) - \mathcal{X}(i, j, k)|, \\ f_{\Theta}(i, j, k) = C \times_1 f_{\theta_1}(i) \times_2 f_{\theta_2}(j) \times_3 f_{\theta_3}(k), \end{aligned} \quad (4)$$

where  $f_{\Theta}(i, j, k)$  denotes the LRTFR [28] that represents the tensor  $\mathcal{X}$  with a Tucker tensor decomposition parameterized by INRs. The loss in (4) is equivalent to using an  $\ell_1$ -norm loss conditioned on the infrared images  $\mathcal{X}$  to optimize a low-rank tensor model, hence the learned tensor  $\mathcal{X}'$  defined by  $\mathcal{X}'(i, j, k) = f_{\Theta}(i, j, k)$  would contain the low-rank background information in the infrared images. We use this coarse background for nonlocal grouping.

Specifically, we conduct nonlocal patch searching using the background tensor  $\mathcal{X}'$ . For each non-overlapping patch tensor  $\mathcal{P}'_l$ , we aim to find its top- $S$  similar patch tensors in the basic patch tensors set  $\{\mathcal{P}'_l\}_{l=1}^L$ . The distance between any two patch tensors is calculated by the Euclidean distance between them. Hence, for each patch  $\mathcal{P}'_l$ , we will find its top- $S$  similar patches in  $\{\mathcal{P}'_l\}_{l=1}^L$ , and we denote the index set of all nonlocal similar patches of  $\mathcal{P}'_l$  as  $I_l$ , which stores all the similar patch indexes of  $\mathcal{P}'_l$ . Then, for each motion-enhanced patch tensor  $\mathcal{P}_l$ , we concat it with other  $S$  patch tensors in  $\{\mathcal{P}_l\}_{l=1}^L$  by using the patch indexes  $I_l$ . These patches would share similar background information due to the nonlocal similarity. Such concat leads to a nonlocal tensor of size  $p \times p \times n_3 \times (S+1)$  for each  $\mathcal{P}_l$ . We then concat all the nonlocal tensors to aggregate them into a five-dimensional tensor  $\mathcal{X}^p \in \mathbb{R}^{L \times p \times p \times n_3 \times (S+1)}$ , where the  $(l, :, :, :)$ -th sub-tensor stores the  $l$ -th key patch  $\mathcal{P}_l$  and its  $S$  nonlocal similar patches (in terms of background similarity) across the spatial-temporal domain. This sub-tensor  $\mathcal{X}^p(l, :, :, :)$  would enjoy strong low-rankness due to its composition of nonlocal similar patches across the infrared images. We illustrate the nonlocal searching algorithm in Algorithm 1.

### 3.5 Nonlocal INR for Background STT Modeling

We conduct the IDSTD fully based on the nonlocal patch dimension of  $\mathcal{X}^p$ . The RPCA framework in Eq. (1) for small target detection in infrared image sequences can be re-formulated in terms of nonlocal patches modeling:

$$\mathcal{X}^p = \mathcal{B}^p + \mathcal{T}^p + \mathcal{N}^p, \quad (5)$$

where  $\mathcal{X}^p, \mathcal{B}^p, \mathcal{T}^p, \mathcal{N}^p \in \mathbb{R}^{L \times p \times p \times n_3 \times (S+1)}$  represent the motion-enhanced patch tensor, the background patch tensor, the target patch tensor and the noise patch tensor, respectively.

By leveraging the nonlocal low-rankness of the background and the sparsity of targets, the detection task can be transformed into an optimization problem to minimize background rank and constrain

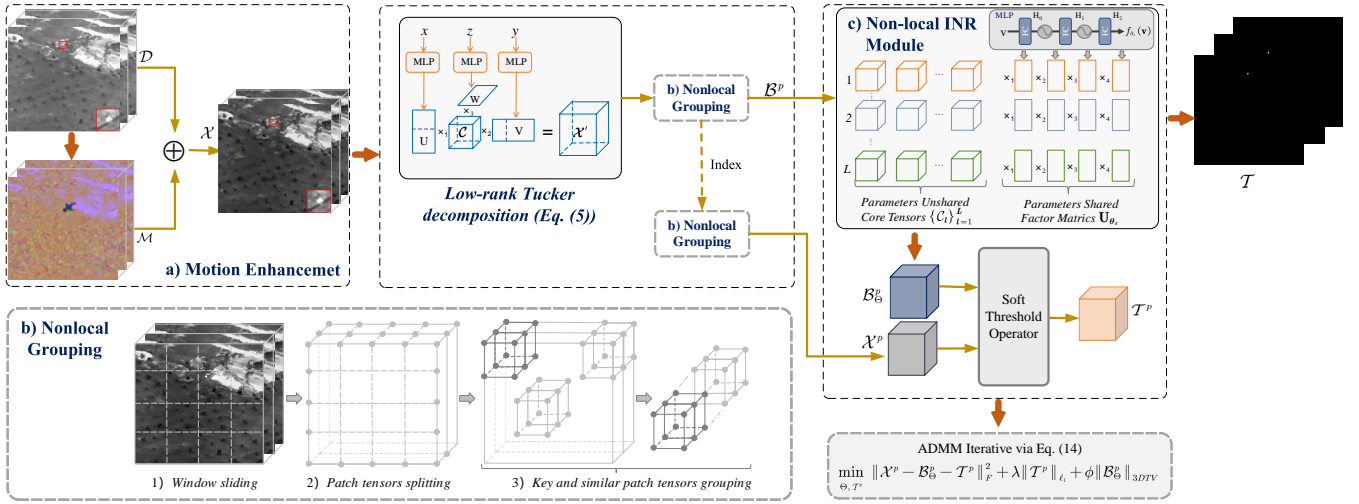


**Figure 2: Overall flowchart of optNL-INR model for IDSTD. a) Motion Enhancement.** This module integrates the original image  $\mathcal{D}$  with the optical flow map  $\mathcal{M}$  to generate an enhanced image  $\mathcal{X}$ . **b) Non-local Grouping.** This module employs a sliding window approach to obtain non-local similar STT models, resulting in patch tensors  $\mathcal{X}^p$  and  $\mathcal{B}^p$ . **c) Non-Local INR.** This module performs implicit neural representation of the background  $\mathcal{B}^p$  in a continuous domain to obtain  $\mathcal{B}_\Theta^p$ . The separated target patch tensor  $\mathcal{T}^p$  is computed via ADMM optimizer and reconstructed into the target image  $\mathcal{T}$ .

**Algorithm 1** Nonlocal patch searching for infrared images

- Input:** The motion-enhanced infrared images  $\mathcal{X}$ ;  
**Output:** The nonlocal similarity aggregated tensor  $\mathcal{X}^p$ ;
- 1: Estimate a coarse background  $\mathcal{X}'$  from  $\mathcal{X}$  using LRTFR (4);
  - 2: Split  $\mathcal{X}$  and  $\mathcal{X}'$  into non-overlapping patches  $\{\mathcal{P}_l \in \mathbb{R}^{p \times p \times n_3}\}_{l=1}^L$  and  $\{\mathcal{P}'_l \in \mathbb{R}^{p \times p \times n_3}\}_{l=1}^L$ ;
  - 3: For each patch  $\mathcal{P}'_l$ , search the top- $S$  nonlocal similar patches in  $\{\mathcal{P}'_l\}_{l=1}^L$  using Euclidean distance, denote  $I_l$  the corresponding nonlocal patch index set;
  - 4: Group each patch  $\mathcal{P}_l$  with  $S$  patches in  $\{\mathcal{P}_l\}_{l=1}^L$  based on the patch index  $I_l$  to form a nonlocal tensor  $p \times p \times n_3 \times (S+1)$ ;
  - 5: Concat these nonlocal tensors of  $\mathcal{X}$  to obtain the nonlocal similarity aggregated tensor  $\mathcal{X}^p \in \mathbb{R}^{L \times p \times p \times n_3 \times (S+1)}$ ;

target sparsity. Furthermore, the noise term  $\mathcal{N}^p$  can be transformed into an  $F$ -norm constraint. Therefore, the optimization problem can be expressed as:

$$\min_{\mathcal{B}^p, \mathcal{T}^p} \|\mathcal{X}^p - \mathcal{B}^p - \mathcal{T}^p\|_F^2 + \text{rank}(\mathcal{B}^p) + \lambda \|\mathcal{T}^p\|_{\ell_1}, \quad (6)$$

where  $\|\cdot\|_{\ell_1}$  denotes the  $\ell_1$ -norm to enforce sparsity. To encode nonlocal low-rankness of background, we introduce a nonlocal INR method, which simultaneously preserves low-rankness and captures spatial-temporal correlations of STT. Meanwhile, we use a soft-thresholding algorithm for dim and small target separation.

Specifically, the nonlocal background patch tensor  $\mathcal{B}^p$  holds strong low-rankness, hence we use the low-rank Tucker decomposition as introduced in Definition 3.2 to model its nonlocal low-rankness. To better capture spatial-temporal correlations of STT, we propose to use INRs [28, 31] to generate the factor matrices of

the nonlocal Tucker decomposition model. The INRs hold inherent global Lipschitz smoothness [28], and hence could implicitly capture the spatial-temporal correlations of STT; see Theorem 3.4. Formally, the nonlocal INR model for the background STT  $\mathcal{B}^p$  is defined as

$$\mathcal{B}_\Theta^p(l, :, :, :, :) := C_l \times_1 U_{\theta_1} \times_2 U_{\theta_2} \times_3 U_{\theta_3} \times_4 U_{\theta_4}, \quad l = 1, \dots, L, \quad (7)$$

$$U_{\theta_d}(i_d, :) = f_{\theta_d}(i_d) \in \mathbb{R}^{r_d}, \quad i_d = 1, \dots, n_d, \quad d = 1, 2, 3, 4,$$

where  $\mathcal{B}_\Theta^p \in \mathbb{R}^{L \times n_1 \times n_2 \times n_3 \times n_4}$  ( $n_1 = n_2 = p, n_4 = S+1$ ) denotes the nonlocal patch tensor of background parameterized by the nonlocal INRs with parameters  $\Theta := \{\{C_l\}_{l=1}^L, \theta_1, \theta_2, \theta_3, \theta_4\}$ . The  $\{C_l\}_{l=1}^L$  are  $L$  unshared core tensors for the  $L$  nonlocal groups. The  $U_{\theta_d} \in \mathbb{R}^{n_d \times r_d}$  denotes the shared factor matrix across all nonlocal groups  $l = 1, \dots, L$ . The shared factor matrix  $U_{\theta_d}$  is generated by the INR network  $f_{\theta_d}(\cdot) : \mathbb{R} \rightarrow \mathbb{R}^{r_d}$ . Such an INR is an MLP with sine activation functions [31], which maps a tensor index  $i_d$  to the corresponding factor vector  $U_{\theta_d}(i_d, :)$ :

$$U_{\theta_d}(i_d, :) = f_{\theta_d}(i_d) = \mathbf{H}_M(\sigma(\mathbf{H}_{M-1} \cdots \sigma(\mathbf{H}_1 i_d))) : \mathbb{R} \rightarrow \mathbb{R}^{r_d}, \quad (8)$$

where  $\theta_d \triangleq \{\mathbf{H}_m\}_{m=1}^M$  are learnable weights of the INR and  $\sigma(\cdot) \triangleq \sin(\omega \cdot)$  denotes the sinusoidal activation function with a frequency parameter  $\omega$  [31]. The strong continuous representation ability of INR makes it effective for generating the nonlocal Tucker model.

The nonlocal INR implicitly exploits the nonlocal low-rankness underlying STT through the tensor decomposition, and hence serves as an effective rank regularization  $\text{rank}(\mathcal{B}^p)$  in (12). The implicit regularization brought by INRs further improves spatial-temporal correlation excavation. Based on the nonlocal INR modeling (7), the proposed IDSTD model is formulated as

$$\min_{\Theta, \mathcal{T}^p} \|\mathcal{X}^p - \mathcal{B}_\Theta^p - \mathcal{T}^p\|_F^2 + \lambda \|\mathcal{T}^p\|_{\ell_1}, \quad (9)$$

where the optimization parameters include the nonlocal INR parameters  $\Theta$  and the sparse target  $\mathcal{T}^p$ .

### 3.6 Theoretical Validation for Nonlocal INR

We first deduce the following theoretical guarantee of the existence of such a nonlocal low-rank INR model (7), given that the background tensor  $\mathcal{B}^p$  holds inherent low-Tucker-rankness features.

**THEOREM 3.3 (EXISTENCE OF THE NONLOCAL INR MODEL).** *Suppose that the factor INR  $f_{\theta_d}(\cdot)$  is an universal approximator over any low-dimensional functions in  $\{f : \mathbb{R} \rightarrow \mathbb{R}^{r_d}\}$  ( $d = 1, 2, 3, 4$ ), then provided that the background nonlocal tensor  $\mathcal{B}^p$  is of low-rank structures, i.e.,  $\text{rank}_T(\mathcal{B}^p(l, :, :, :)) \leq (r_1, r_2, r_3, r_4)$  for any  $l$ , then there must exist a group of parameters  $\Theta := \{\{C_l\}_{l=1}^L, \theta_1, \theta_2, \theta_3, \theta_4\}$  that satisfy  $\mathcal{B}^p(l, i_1, i_2, i_3, i_4) = C_l \times_1 f_{\theta_1}(i_1) \times_2 f_{\theta_2}(i_2) \times_3 f_{\theta_3}(i_3) \times_4 f_{\theta_4}(i_4)$ .*

**PROOF.** The conjecture directly follows from the combination of (1) the existence property of the low-rank tensor function factorization in Theorem 2 of [28], by viewing each  $\mathcal{B}^p(l, :, :, :)$  as a discrete tensor sampled on a low-rank tensor function with function rank less than  $(r_1, r_2, r_3, r_4)$ , and (2) the universal approximation of the INR for representing any functions on the Euclidean space.

The existence result justifies the rationality of using the nonlocal INR for background modeling in infrared images, since the nonlocal-enhanced background tensor  $\mathcal{B}^p$  usually enjoys strong low-rankness, and the nonlocal INR could losslessly represent this low-rank background. Moreover, the nonlocal INR implicitly captures the global spatial-temporal correlations in infrared images by the continuous function representation of INRs, thereby enhancing the performance for IDSTD. We establish the theoretical implicit regularization of our model as follows.

**THEOREM 3.4.** *Let  $f_{\theta_1}(\cdot), f_{\theta_2}(\cdot), f_{\theta_3}(\cdot), f_{\theta_4}(\cdot)$  be factor INRs with sine activation function  $\sin(\omega \cdot)$  and depth  $M$ . Assume that the  $\ell_1$ -norm of each core tensor  $C_l$  ( $l = 1, 2, \dots, L$ ) and each weight matrix of factor INRs is bounded by  $\eta$ . Denote the background patch tensor generated by such nonlocal INRs as  $\mathcal{B}^p(l, i_1, i_2, i_3, i_4) = C_l \times_1 f_{\theta_1}(i_1) \times_2 f_{\theta_2}(i_2) \times_3 f_{\theta_3}(i_3) \times_4 f_{\theta_4}(i_4)$ . Then, we have the following smoothness bound that reveals the global spatial-temporal correlation:*

$$\begin{aligned} & |\mathcal{B}^p_{\Theta}(l_1, i_1, \dots, i_d, \dots, i_d) - \mathcal{B}^p_{\Theta}(l_2, i_1, \dots, i'_d, \dots, i_d)| \\ & \leq \delta_1 |i_d - i'_d| + \delta_2, \end{aligned} \quad (10)$$

where  $\delta_1, \delta_2$  are constants. The inequality holds for any two nonlocal groups  $l_1, l_2 \in \{1, 2, \dots, L\}$ , dimension  $d \in \{1, 2, 3, 4\}$ , and tensor indexes  $i_d, i'_d$ . When  $l_1 = l_2$ , the upper bound reduces to  $\delta_1 |i_d - i'_d|$ .

The proof of Theorem 3.4 is placed in Section 4.1. Theorem 3.4 indicates that the nonlocal INR model captures global spatial-temporal correlations underlying the background of infrared images by bounding the differences between spatial-temporal elements of  $\mathcal{B}^p_{\Theta}$  with some constants. This bound is intrinsically related to the Lipschitz continuous nature of the INR [28]. Especially, the nonlocal INR model differentiates between intra- and inter-relationships within nonlocal groups  $\{\mathcal{B}^p_{\Theta}(l, :, :, :)\}_{l=1}^L$ , i.e., the intra-relationships inside a group (when  $l_1 = l_2$ ) is more pronounced than the inter-relationships between different nonlocal groups (when  $l_1 \neq l_2$ ). This theoretical result interprets the ability of nonlocal INRs to simultaneously characterize the nonlocal low-rankness and the intrinsic

spatial-temporal correlation of infrared images background in a flexible way, where such characterizations are adaptively learned through a parametric nonlocal INR model (7).

### 3.7 3DTV and ADMM Algorithm for IDSTD

To more faithfully capture spatial-temporal local correlations of the background, we further introduce a spatial-temporal 3D total variation regularization into the model:

$$\left\| \mathcal{B}^p_{\Theta} \right\|_{3DTV} = \left\| \nabla_x \left( \mathcal{B}^p_{\Theta} \right) \right\|_{\ell_1} + \left\| \nabla_y \left( \mathcal{B}^p_{\Theta} \right) \right\|_{\ell_1} + \eta \left\| \nabla_z \left( \mathcal{B}^p_{\Theta} \right) \right\|_{\ell_1}, \quad (11)$$

where  $\eta$  is a weight parameter used to emphasize the importance of temporal information, and  $\nabla_x, \nabla_y, \nabla_z$  are first-order difference operators for a tensor along different dimensions. The optimization problem in Eq. (9) can be further expressed as:

$$\min_{\Theta, \mathcal{T}^p} \left\| \mathcal{X}^p - \mathcal{B}^p_{\Theta} - \mathcal{T}^p \right\|_F^2 + \lambda \left\| \mathcal{T}^p \right\|_{\ell_1} + \phi \left\| \mathcal{B}^p_{\Theta} \right\|_{3DTV}, \quad (12)$$

where  $\phi$  is a trade-off parameter of the regularization. To address the optimization model (12), we employ an auxiliary variable  $\mathcal{A}$  and a Lagrange multiplier  $\Lambda$ , and transform the global optimization into several subproblems under the alternating direction method of multipliers (ADMM) framework:

$$\begin{aligned} & \min_{\mathcal{A}} \left\| \mathcal{X}^p - \mathcal{A} - \mathcal{T}^p \right\|_F^2 + \frac{\rho_t}{2} \left\| \mathcal{A} - \mathcal{B}^p_{\Theta_t} + \Lambda_t \right\|_F^2, \\ & \min_{\Theta} \frac{\rho_t}{2} \left\| \mathcal{A}_{t+1} - \mathcal{B}^p_{\Theta} + \Lambda_t \right\|_F^2 + \phi \left\| \mathcal{B}^p_{\Theta} \right\|_{3DTV}, \\ & \min_{\mathcal{T}^p} \left\| \mathcal{X}^p - \mathcal{A}_{t+1} - \mathcal{T}^p \right\|_F^2 + \lambda \left\| \mathcal{T}^p \right\|_{\ell_1}, \\ & \Lambda_{t+1} = \Lambda_t + \mathcal{A}_{t+1} - \mathcal{B}^p_{\Theta_{t+1}}, \quad \rho_{t+1} = \kappa \rho_t, \end{aligned} \quad (13)$$

where  $\kappa > 1$  is a constant under the ADMM framework,  $t$  denotes the index of iteration number, and  $\rho_t$  is a trade-off parameter that evolves with iterations. Here, the  $\mathcal{A}$ -subproblem consists of squared terms and can be solved by first-order optimal condition. The  $\Theta$ -subproblem is optimized through utilizing the Adam [15] optimizer in each iteration of the ADMM, which is viewed as a plug-and-play denoising subproblem under the ADMM framework. The sparse target  $\mathcal{T}^p$ -subproblem is employed to accurately separate and extract the target from the background. It can be solved efficiently by the soft threshold shrinkage operator [10]:

$$\mathcal{T}^p_{t+1} = \mathcal{S}_{\frac{\lambda}{2}} \left( \mathcal{X}^p - \mathcal{A}_{t+1} \right), \quad (14)$$

where  $\mathcal{S}(\cdot)$  represents the soft-thresholding shrinkage operator defined as  $\mathcal{S}_{\xi}(x) = \text{sign}(x) \cdot \max(|x| - \xi, 0)$ , where  $\xi$  is the threshold value. Under mild assumptions of bounded denoiser [3], we have the following fixed-point convergence guarantee for the plug-and-play ADMM algorithm, whose proof is in Section 4.2.

**LEMMA 3.5.** *Assume that the  $\Theta$ -subproblem in (13) is a bounded denoiser, i.e.,  $\left\| \mathcal{B}^p_{\Theta_{t+1}} - (\mathcal{A}_{t+1} + \Lambda_t) \right\|_F^2 \leq \frac{C}{\rho^t}$  for a constant  $C$ . Then the iterates in (13) admit a fixed-point convergence, i.e., there exist  $(\mathcal{A}^*, \Theta^*, \Lambda^*)$  such that  $\left\| \mathcal{A}_t - \mathcal{A}^* \right\|_F^2 \rightarrow 0$ ,  $\left\| \mathcal{B}^p_{\Theta_t} - \mathcal{B}^p_{\Theta^*} \right\|_F^2 \rightarrow 0$ , and  $\left\| \Lambda_t - \Lambda^* \right\|_F^2 \rightarrow 0$  as  $t \rightarrow \infty$ .*

After the optimization of ADMM, we reshape the optimized sparse target  $\mathcal{T}^p \in \mathbb{R}^{L \times p \times p \times n_3 \times (S+1)}$  to the original STT shape  $n_1 \times n_2 \times n_3$  to obtain the IDSTD result.

## 4 Proof

### 4.1 Proof of Theorem 3.4

PROOF. For any  $l_1, l_2$ , we compute:

$$\begin{aligned} & \left| \mathcal{B}_{\Theta}^p(l_1, i_1, \dots, i_d, \dots, i_d) - \mathcal{B}_{\Theta}^p(l_2, i_1, \dots, i'_d, \dots, i_d) \right| \\ &= \left| \left( C_{l_1} \times_d f_{\theta_d}(i_d) - C_{l_2} \times_d f_{\theta_d}(i'_d) \right) \times_1 f_{\theta_1}(i_1) \cdots \times_d f_{\theta_d}(i_d) \right| \\ &\leq \|C_{l_1} \times_d f_{\theta_d}(i_d) - C_{l_2} \times_d f_{\theta_d}(i'_d)\|_{\ell_1} \prod_{k \neq d} \|f_{\theta_k}(i_k)\|_{\ell_1} \\ &\leq \|C_{l_1} \times_d f_{\theta_d}(i_d) - C_{l_2} \times_d f_{\theta_d}(i'_d)\|_{\ell_1} \eta^{3M} \omega^{3(M-1)} \xi^3. \end{aligned}$$

Decompose the tensor difference:

$$\begin{aligned} & \|C_{l_1} \times_d f_{\theta_d}(i_d) - C_{l_2} \times_d f_{\theta_d}(i'_d)\|_{\ell_1} \\ &= \|C_{l_1} \times_d f_{\theta_d}(i_d) - C_{l_2} \times_d f_{\theta_d}(i_d) + C_{l_2} \times_d f_{\theta_d}(i_d) - C_{l_2} \times_d f_{\theta_d}(i'_d)\|_{\ell_1} \\ &\leq 2\eta \|f_{\theta_d}(i_d)\|_{\ell_1} + \eta \|f_{\theta_d}(i_d) - f_{\theta_d}(i'_d)\|_{\ell_1}. \end{aligned} \quad (15)$$

Using the boundedness of INRs with  $\sin(\omega \cdot)$ :

$$\|f_{\theta_k}(i_k)\|_{\ell_1} \leq \eta^M \omega^{M-1} |i_k|, \quad \|f_{\theta_d}(i_d) - f_{\theta_d}(i'_d)\|_{\ell_1} \leq \eta^M \omega^{M-1} |i_d - i'_d|.$$

Let  $\xi = \max\{|i_1|, \dots, |i_d|, |i'_d|, \dots, |i_d|\}$ . Combining all bounds:

$$\begin{aligned} & \left| \mathcal{B}_{\Theta}^p(l_1, i_1, \dots, i_d, \dots, i_d) - \mathcal{B}_{\Theta}^p(l_2, i_1, \dots, i'_d, \dots, i_d) \right| \\ &\leq \left( 2\eta^{M+1} \omega^{M-1} \xi + \eta^{M+1} \omega^{M-1} |i_d - i'_d| \right) \eta^{3M} \omega^{3(M-1)} \xi^3 \\ &= \delta_1 |i_d - i'_d| + \delta_2, \end{aligned}$$

where  $\delta_1 = \eta^{4M+1} \omega^{4(M-1)} \xi^3$  and  $\delta_2 = 2\eta^{4M+1} \omega^{4(M-1)} \xi^4$ . When  $l_1 = l_2$ , the  $\delta_2$ -term vanishes because the  $2\eta \|f_{\theta_d}(i_d)\|_{\ell_1}$  term in (15) vanishes. This completes the proof.

### 4.2 Proof of Lemma 3.5

PROOF. We demonstrate that  $(\mathcal{B}_{\Theta_t}^p, \mathcal{A}_t, \Lambda_t)$  forms a Cauchy sequence with iteratively decreasing constants. Specifically, we bound the differences between consecutive iterates as follows:

$$\begin{aligned} \|\mathcal{B}_{\Theta_{t+1}}^p - \mathcal{B}_{\Theta_t}^p\|_F &= D_{\mathcal{B}_{\Theta}}^t, \\ \|\mathcal{A}_{t+1} - \mathcal{A}_t\|_F &= D_{\mathcal{A}}^t, \\ \|\Lambda_{t+1} - \Lambda_t\|_F &= D_{\Lambda}^t, \end{aligned} \quad (16)$$

where  $D_{\mathcal{B}_{\Theta}}^t, D_{\mathcal{A}}^t$ , and  $D_{\Lambda}^t$  decay as  $\rho_t$  increases. Using the triangle inequality and the bounded denoiser assumption:

$$\begin{aligned} \|\mathcal{B}_{\Theta_{t+1}}^p - \mathcal{B}_{\Theta_t}^p\|_F &\leq \|\mathcal{B}_{\Theta_{t+1}}^p - (\mathcal{A}_{t+1} + \Lambda_t)\|_F + \|(\mathcal{A}_{t+1} + \Lambda_t) - \mathcal{B}_{\Theta_t}^p\|_F \\ &\leq \sqrt{\frac{C}{\rho_t}} + \|\mathcal{A}_{t+1} - \mathcal{B}_{\Theta_t}^p + \Lambda_t\|_F. \end{aligned} \quad (17)$$

From the  $\mathcal{A}$ -subproblem optimality:

$$\|\mathcal{A}_{t+1} - \mathcal{B}_{\Theta_t}^p + \Lambda_t\|_F = \frac{2}{\rho_t} \|\mathcal{X}^p - \mathcal{A}_{t+1} - \mathcal{T}^p\|_F. \quad (18)$$

Since  $\|\mathcal{X}^p - \mathcal{A} - \mathcal{T}^p\|_F \leq \|\mathcal{X}^p\|_F + \|\mathcal{A}\|_F + \|\mathcal{T}^p\|_F \triangleq D'$  from the element-wise boundedness in  $[0, 1]$ , we have:

$$\|\mathcal{B}_{\Theta_{t+1}}^p - \mathcal{B}_{\Theta_t}^p\|_F \leq \sqrt{\frac{C}{\rho_t}} + \frac{2D'}{\rho_t} \leq \frac{\sqrt{C} + 2D'}{\sqrt{\rho_t}}. \quad (19)$$

Using the update rule for  $\Lambda$ :

$$\begin{aligned} \|\Lambda_{t+1} - \Lambda_t\|_F &\leq \|\Lambda_{t+1}\|_F + \|\Lambda_t\|_F \\ &= \|\Lambda_t + \mathcal{A}_{t+1} - \mathcal{B}_{\Theta_{t+1}}^p\|_F + \|\Lambda_{t-1} + \mathcal{A}_t - \mathcal{B}_{\Theta_t}^p\|_F \\ &\leq 2\sqrt{\frac{C}{\rho_t}}. \end{aligned} \quad (20)$$

Expressing the difference using the  $\Lambda$  updates:

$$\begin{aligned} \|\mathcal{A}_{t+1} - \mathcal{A}_t\|_F &\leq \|\Lambda_{t+1} - \Lambda_t\|_F + \|\Lambda_t - \Lambda_{t-1}\|_F \\ &\quad + \|\mathcal{B}_{\Theta_{t+1}}^p - \mathcal{B}_{\Theta_t}^p\|_F \\ &\leq 4\sqrt{\frac{C}{\rho_t}} + \frac{\sqrt{C} + 2D'}{\sqrt{\rho_t}} = \frac{5\sqrt{C} + 2D'}{\sqrt{\rho_t}}. \end{aligned} \quad (21)$$

Since  $\rho_{t+1} = \kappa \rho_t$  with  $\kappa > 1$ ,  $\rho_t \rightarrow \infty$  as  $t \rightarrow \infty$ . Thus, all bounds  $D_{\mathcal{B}_{\Theta}}^t, D_{\mathcal{A}}^t$ , and  $D_{\Lambda}^t$  decay to zero. This implies  $(\mathcal{B}_{\Theta_t}^p, \mathcal{A}_t, \Lambda_t)$  is a Cauchy sequence and converges to a fixed point  $(\mathcal{B}_{\Theta^*}^p, \mathcal{A}^*, \Lambda^*)$ . Therefore,  $\|\mathcal{A}_t - \mathcal{A}^*\|_F^2 \rightarrow 0$ ,  $\|\mathcal{B}_{\Theta_t}^p - \mathcal{B}_{\Theta^*}^p\|_F^2 \rightarrow 0$ , and  $\|\Lambda_t - \Lambda^*\|_F^2 \rightarrow 0$  as  $t \rightarrow \infty$ .

## 5 Experiments

### 5.1 Experiment Setup

**Datasets.** We conduct experiments on two public datasets for time-continues IDSTD task: ATR<sup>1</sup> and Anti-UAV<sup>2</sup>.

**ATR** The ground/air background infrared detection and tracking dataset was publicly released by the ATR Key Laboratory of the National University of Defense Technology between 2017 and 2019. It consists of 22 image sequences, totaling 16,177 frames and 16,944 targets. Each sequence is accompanied by a label file indicating the target locations. The images were captured with medium-wave infrared (3–5  $\mu\text{m}$ ) equipment, with a resolution of 256×256 pixels. For simplicity, this dataset is referred to as dataset A.

**Anti-UAV** The dataset was released by the 4th Anti-UAV workshop and challenge at CVPR 2025, and we utilize the data from track 1. The dataset consists of 410 video sequences for three tracks in total, addressing the scarcity of high-quality benchmarks in dynamic environments. The sequences exhibit a wide range of complex scenarios, including clouds, buildings, mountains, and forests. For simplicity, this dataset is referred to as dataset B.

It is particularly noted that only centroid labels are available for the two datasets, which limits the evaluation of detection performance. To address this limitation, we propose a centroid-guided clustering approach to generate non-centroid (i.e., contour-level or region-level) annotations. This method enables a more accurate assessment of an algorithm's ability to predict both the location and shape of targets. We have released the code, which is available at <https://github.com/franciswang-0126/CGRCA/tree/main>.

**Metrics.** The performance assessment of the algorithms is achieved by calculating the intersection over union (*IoU*), Fmeasure ( $F_1$ ), probability of detection ( $P_d$ ), and false-alarm rate ( $F_a$ ). We introduce the used metrics as follows.

<sup>1</sup><http://www.sciencedb.cn/dataSet/handle/902>

<sup>2</sup><https://codalab.lisn.upsaclay.fr/competitions/21688>

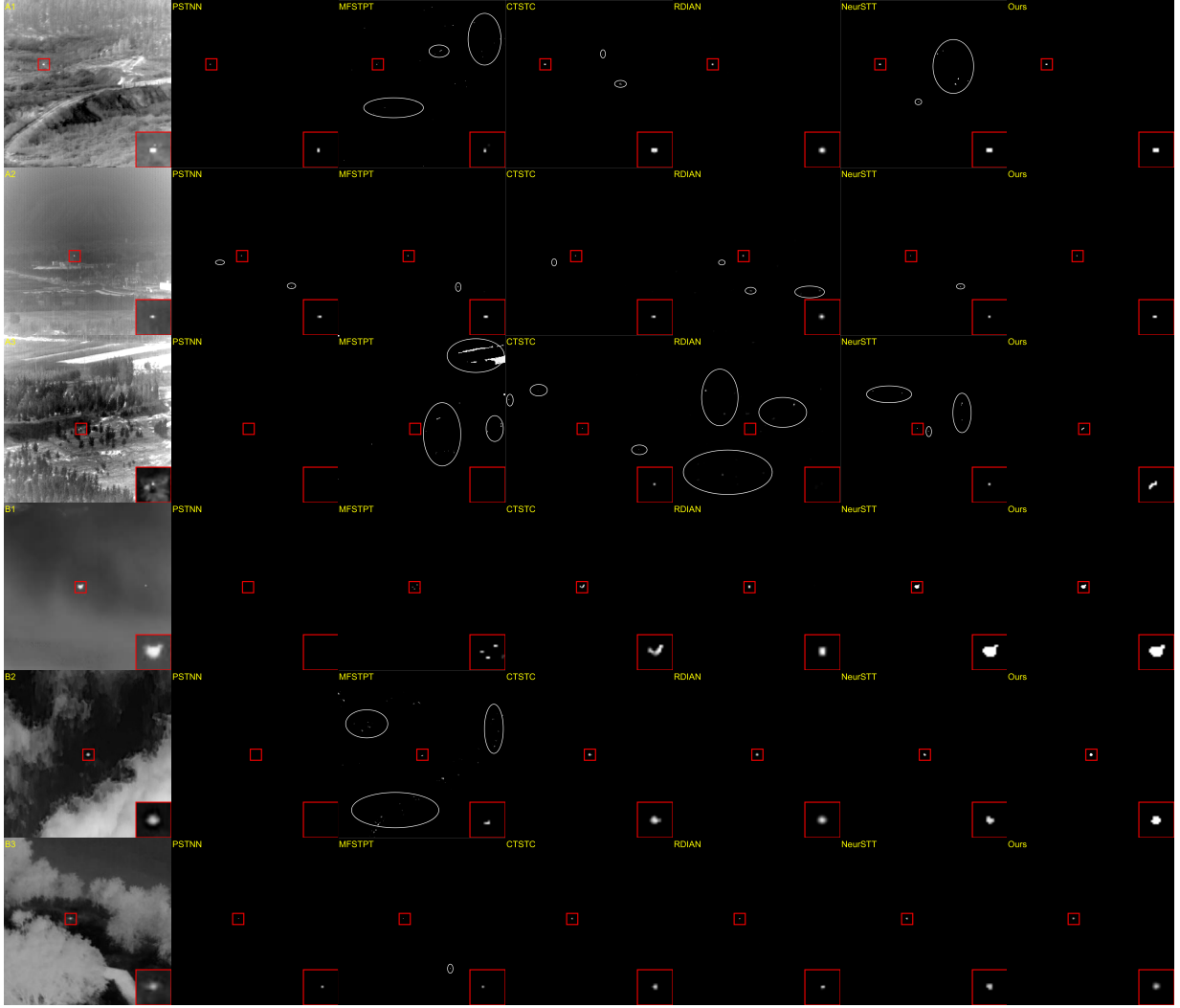


**Figure 3: Visual results from different methods in datasets A1-A3, and B1-B3. The target regions and false alarms are marked with red boxes and white circles, respectively.**

The metric  $IoU$  quantifies the ratio of intersection areas  $A_{inter}$  and union areas  $A_{union}$  between the detections and labels, and  $F_1$  quantifies the relationship between *Precision* and *Recall*. Both of these metrics are pixel-based, defined as follows:

$$IoU = \frac{A_{inter}}{A_{union}}, F_1 = \frac{2 \times Precision \times Recall}{Precision + Recall}. \quad (22)$$

The metric  $P_d$  quantifies the ratio of correctly predicted target number  $T_{correct}$  over all target number  $T_{All}$ , and  $F_a$  measures the ratio of falsely predicted pixels  $P_{false}$  over all image pixels  $P_{All}$ . These two metrics are target-level, defined as follows:

$$P_d = \frac{T_{correct}}{T_{All}}, F_a = \frac{P_{false}}{P_{All}}. \quad (23)$$

**Implement Details.** We implement our method on an Nvidia GeForce 3090 GPU, and adopt the Adam optimizer [15] with learning rate of 0.0001 and decay rate of 0.01 in the  $\Theta$ -subproblem. Experiments on traditional methods are conducted using Matlab R2023a.

## 5.2 Parameters Analysis

We conducted critical parameters tests on typical scenes and analyze the variation trend of average  $IoU$ , as shown in Figure 4.

**Balancing Parameter  $\lambda$ :** It is a trade-off factor balancing the target and background. A larger value yields a cleaner target but causes excessive shrinkage, while a smaller value preserves targets but retains background clutter. We vary  $\lambda$  in  $\{0.20, 0.23, 0.25, 0.28, 0.30\}$  and set  $\lambda = 0.25$  for optimal performance.

**Rank of The Patch Tensor:** Low-rank constraints on patch tensors help preserve structural details and suppress high-frequency

**Table 1: Detailed parameter settings of the comparison methods.**

Methods	Parameter Settings
NOLC [48]	$L = 1, H = 0.5, p = 30, s = 10, \lambda = L/\sqrt{\max(n_1, n_2)} \times n_3$
NRAM [42]	$p = 50, s = 10, \lambda = 1/\sqrt{\min(n_1, n_2)}, \mu_0 = 3L, \gamma = 0.002, C = \frac{1}{2.5\lambda}, \varepsilon = 10^{-7}$
NTFRA [17]	$p = 40 \times 40, s = 40, \lambda = 3/\sqrt{\max(n_1, n_2)} \times n_3, \beta = 10^{-4}, \varepsilon = 10^{-4}$
PSTNN [43]	$p = 60 \times 60, s = 60, \lambda = 1/\sqrt{\max(n_1, n_2)} \times n_3, \mu = 3 \times 10^{-3}, \varepsilon = 10^{-7}$
SRWS [47]	$p = 50, s = 10, \beta = 1/\sqrt{\min(n_1, n_2)}, \lambda = \lambda_L/\sqrt{\min(n_1, n_2)}, \gamma = \gamma_L/\sqrt{\min(n_1, n_2)}$
ASTTV-NTLA [23]	$L = 3, \lambda_{tv} = 0.005, \lambda_s = 10/\sqrt{\max(m, n)} \times L, \lambda_3 = 100$
IMNN-LWEC [25]	$p = 15 \times 15, s = 15, L = 3, \omega = 5, \lambda_1 = 10^5 \times 2/\sqrt{\max(n_1, n_2)} \times n_3, \lambda_2 = 50\lambda_1, \beta_{k_1 k_2} = \rho = 1/\omega$
MFSTPT [13]	$p = 60 \times 60, s = 60, \lambda = 1/\sqrt{\max(n_1, n_2)} \times n_3$
NFTDGSTV [22]	$C = 5, L = 3, H = 4, \lambda_1 = 0.01, \lambda_2 = H/\sqrt{\max(n_1, n_2)} \times n_3, \lambda_3 = 0.001$
TCTV [21]	$p = 60 \times 60, s = 60, \lambda = 12/\sqrt{\max(n_1, n_2)} \times n_3, \beta = 3/\sqrt{\min(n_1, n_2)}, \mu = 0.001, \varepsilon = 10^{-2}$
CTSTC [26]	$f = 3, \lambda_L = 30, \mu = 0.01, \eta = 1.0, \lambda_1 = \lambda_L/\sqrt{\max(n_1, n_2)} \times n_3, \lambda_2 = 80\lambda_1, \lambda_3 = 10\lambda_1, \gamma = 0.5, \delta = 10^{-4}$
NeurSTT [35]	$L = 80, \lambda = 0.2, \phi = 5 \times 10^{-5}, \kappa = 100, k_{\max} = 2000$
Ours	$L = 100, \lambda = 0.25, \phi = 1 \times 10^{-6}, k_{\max} = 1500, p = 64, s = 64, W = 15, \sigma = 0.8$

**Table 2: Quantitative results on datasets A1-A4 produced by different methods in  $IoU$  ( $10^{-2}$ ),  $F_1$  ( $10^{-2}$ ),  $P_d$  ( $10^{-2}$ ) and  $F_a$  ( $10^{-5}$ ) under Tr=40%. The average running time (s) per frame is reported.**

Methods	Category	A1				A2				A3				A4				Avg Time
		$IoU$	$F_1$	$P_d$	$F_a \downarrow$	$IoU$	$F_1$	$P_d$	$F_a \downarrow$	$IoU$	$F_1$	$P_d$	$F_a \downarrow$	$IoU$	$F_1$	$P_d$	$F_a \downarrow$	
NOLC [48]	single-Opti	42.34	52.07	85.00	2.55	44.16	61.27	69.00	3.71	8.86	16.28	54.00	17.09	53.75	69.92	86.00	6.27	0.782
NRAM [42]	single-Opti	17.14	29.27	61.00	1.79	65.13	78.88	71.00	1.31	32.46	49.01	84.00	2.12	10.43	18.89	49.00	1.82	1.237
NTFRA [17]	single-Opti	39.21	56.34	72.00	12.70	2.19	4.29	54.00	12.03	0.04	0.07	16.00	730.67	81.32	89.70	88.00	1.40	1.466
PSTNN [43]	single-Opti	16.34	28.10	64.00	1.12	63.49	77.67	76.00	1.34	18.82	31.67	32.50	1.89	26.43	41.82	92.00	2.79	0.443
SRWS [47]	single-Opti	29.04	45.01	69.00	1.29	72.45	84.43	79.00	0.98	26.97	42.48	60.00	1.72	33.00	49.63	91.00	1.67	0.832
ASTTV [23]	multi-Opti	32.95	49.56	76.00	12.80	31.71	48.16	72.00	2.66	8.54	15.74	85.50	17.09	63.88	77.96	89.00	2.75	1.839
IMNN [25]	multi-Opti	59.04	74.24	93.00	0.86	61.29	76.00	81.00	0.08	0.00	0.00	0.00	9.55	81.29	89.68	93.00	0.69	2.299
MFSTPT [13]	multi-Opti	16.44	28.24	92.00	13.23	16.59	28.46	85.00	6.36	6.15	11.59	66.00	14.95	23.11	37.54	79.00	7.87	19.65
NFTDGSTV [22]	multi-Opti	72.16	84.27	97.00	0.86	58.54	73.85	98.00	0.15	0.00	17.00	75.00	16.50	77.69	87.45	98.00	0.85	1.858
TCTV [21]	multi-Opti	75.45	85.92	98.00	0.98	77.49	87.32	97.00	0.34	34.27	49.06	89.00	4.32	74.00	85.06	96.00	1.36	2.592
CTSTC [26]	multi-Opti	75.78	86.22	98.00	2.27	73.59	84.79	94.00	0.61	3.51	6.77	82.00	42.30	72.51	84.06	90.00	3.53	0.146
ACM [7]	single-DL	16.67	28.57	90.00	26.17	0.65	1.28	9.00	15.70	0.00	0.00	0.00	4.03	25.08	40.11	63.00	4.73	0.113
ALCNet [8]	single-DL	28.75	44.66	77.00	1.68	0.85	1.68	16.00	38.94	0.00	0.00	0.00	8.07	18.71	31.52	49.00	6.30	0.098
PBT [41]	single-DL	28.95	44.90	89.00	0.90	77.06	87.04	100.0	0.09	9.51	17.36	49.50	6.96	2.53	4.93	21.00	2.84	0.132
RDIAN [32]	single-DL	14.83	25.82	42.00	1.43	77.82	87.53	100.0	0.43	12.33	21.95	24.00	1.39	0.37	0.74	4.00	2.93	0.097
RPCANet [36]	single-DL	7.70	14.30	34.00	1.50	44.69	61.77	100.0	3.22	10.18	18.47	27.00	2.40	3.12	6.04	32.00	1.69	0.112
NeurSTT [35]	multi-DL	72.30	83.93	96.00	2.27	74.79	85.58	96.00	0.41	24.88	39.84	90.50	4.15	82.52	90.43	94.00	1.05	0.587
optNL-INR	multi-DL	77.25	87.17	99.00	0.57	83.81	91.19	99.00	0.02	65.89	79.44	98.00	0.02	83.17	90.81	100.0	0.57	0.607

noise. A higher rank relaxes the constraint and preserves target integrity, while a lower rank may diminish the target. We vary  $r_1$  and  $r_2$  in  $\{12, 14, 16, 18, 20\}$ ,  $r_3$  in  $\{5, 10, 15, 20, 25\}$ , and  $r_4$  in  $\{4, 5, 6, 7, 8\}$ , and set  $(r_1, r_2, r_3, r_4) = (16, 16, 15, 6)$  for optimal performance.

**Patch Size  $p$** : It affects non-local similarity representation. A larger value improves target sparsity but introduces more background noise, while a smaller one weakens sparsity. We vary the patch size in  $\{6, 8, 16, 32, 64\}$  and set  $p = 64$  for optimal performance.

**Optical Window Size**: It is used in optical flow computation. A larger value improves robustness to motion noise but reduces sensitivity to small targets, while a smaller one captures local motion better but is more noise-sensitive. We vary the window size in  $\{5, 8, 10, 12, 15\}$  and set it to 15 for optimal performance.

**Regularization Term Coefficient  $\phi$** : It is the coefficient of 3DTV regularization for determining the constraints on spatial-temporal features. A larger value can emphasize spatial-temporal

information, but may introduce unnecessary noise interference. Conversely, a smaller value reduces the constraints on spatial-temporal features, but increases the risk of target loss. We vary  $\phi$  in  $\{5e^{-5}, 1e^{-5}, 5e^{-6}, 1e^{-6}, 5e^{-7}\}$ . To achieve optimal performance, we set  $\phi = 1e^{-6}$ .

**Network Width**: The width of nonlinear networks affects the performance of INRs for low-rank background estimation. Larger network widths are prone to overfitting, while smaller network widths limit the algorithm’s performance. We vary the network width in  $\{16, 32, 64, 128, 256\}$ . To achieve optimal performance, we set the network width to 64, consistent with the patch size.

**Number of Similar Blocks  $S$** : It also affects the ability of non-local representations. A larger value introduces extra information and increases computational complexity, while a smaller value leads to insufficient representation of non-local similarity features. We

**Table 3: Quantitative results on datasets A5-A6 and B1-B2 produced by different methods in  $IoU$  ( $10^{-2}$ ),  $F_1$  ( $10^{-2}$ ),  $P_d$  ( $10^{-2}$ ) and  $F_a$  ( $10^{-5}$ ) under Tr=40%. The average running time (s) per frame is reported.**

Methods	Category	A5				A6				B1				B2				Avg Time
		$IoU$	$F_1$	$P_d$	$F_a \downarrow$	$IoU$	$F_1$	$P_d$	$F_a \downarrow$	$IoU$	$F_1$	$P_d$	$F_a \downarrow$	$IoU$	$F_1$	$P_d$	$F_a \downarrow$	
NOLC [48]	single-Opti	21.84	35.84	72.00	7.11	49.64	62.11	78.00	0.57	9.03	16.56	65.00	8.99	50.92	65.72	90.00	0.98	0.730
NRAM [42]	single-Opti	5.57	10.55	32.00	1.29	46.98	60.23	73.00	0.63	9.49	17.34	61.00	2.95	5.25	9.98	45.00	2.49	1.180
NTFRA [17]	single-Opti	2.49	4.85	89.00	32.91	3.19	6.19	77.00	62.24	35.02	51.87	96.00	1.67	11.42	20.49	50.00	1.91	1.458
PSTNN [43]	single-Opti	15.10	26.24	75.00	1.72	49.04	71.68	74.00	0.29	2.56	4.98	25.00	8.90	6.31	11.88	59.00	0.58	0.422
SRWS [47]	single-Opti	14.62	25.51	55.00	1.43	62.97	74.38	80.00	0.66	10.00	18.18	78.00	3.69	29.12	45.11	92.00	1.19	0.816
ASTTV [23]	multi-Opti	0.74	1.47	86.00	19.91	37.04	54.05	79.00	3.02	0.59	1.18	66.00	200.6	0.71	1.41	65.00	100.6	1.827
IMNN [25]	multi-Opti	33.47	50.15	88.00	11.12	14.02	24.59	64.00	7.60	44.63	61.71	95.00	1.05	59.48	74.60	89.00	0.76	2.295
MFSTPT [13]	multi-Opti	17.05	29.14	83.00	9.95	10.36	18.78	67.00	12.97	10.11	18.36	65.00	5.55	12.20	21.75	81.00	7.20	17.48
NFTDGSTV [22]	multi-Opti	31.52	47.94	78.00	8.82	25.69	40.88	78.00	5.57	36.28	53.24	95.00	0.98	46.94	63.89	91.00	0.53	1.833
TCTV [21]	multi-Opti	44.36	61.46	90.00	4.52	55.67	71.52	76.00	0.14	42.34	59.49	97.00	0.95	34.62	51.43	93.00	0.26	2.374
CTSTC [26]	multi-Opti	43.59	60.72	93.00	5.84	61.63	73.47	80.00	0.90	42.42	59.57	98.00	2.32	61.43	76.11	90.00	0.64	0.143
ACM [7]	single-DL	8.29	15.31	19.00	5.28	0.45	0.89	3.00	4.26	17.93	30.41	47.00	23.45	43.14	60.28	93.00	8.12	0.105
ALCNet [8]	single-DL	15.88	27.41	36.00	10.93	0.11	0.23	2.00	10.82	37.65	54.71	66.00	3.86	44.96	62.03	92.00	2.35	0.093
PBT [41]	single-DL	3.82	7.35	70.00	29.51	31.77	48.22	93.00	3.11	2.57	5.00	18.00	4.21	0.65	1.30	96.00	652.1	0.128
RDIAN [32]	single-DL	5.75	10.87	17.00	2.56	8.44	15.56	79.00	0.15	0.00	0.00	0.00	7.84	6.67	12.50	27.00	17.29	0.092
RPCANet [36]	single-DL	8.64	15.91	54.00	1.54	63.13	74.48	85.00	0.15	17.27	29.46	26.00	6.70	1.27	2.51	9.00	55.42	0.109
NeurSTT [35]	multi-DL	49.41	66.14	88.00	0.75	52.02	68.43	84.00	1.43	49.75	66.44	96.00	1.27	58.69	73.97	94.00	0.37	0.583
optNL-INR	multi-DL	<b>52.03</b>	<b>68.45</b>	<b>97.00</b>	<b>0.66</b>	<b>64.46</b>	<b>78.39</b>	<b>86.00</b>	<b>0.02</b>	<b>66.55</b>	<b>79.92</b>	<b>99.00</b>	<b>0.90</b>	<b>65.73</b>	<b>79.32</b>	<b>100.0</b>	<b>0.25</b>	<b>0.604</b>

**Table 4: Quantitative results on datasets B3-B6 produced by different methods in  $IoU$  ( $10^{-2}$ ),  $F_1$  ( $10^{-2}$ ),  $P_d$  ( $10^{-2}$ ) and  $F_a$  ( $10^{-5}$ ) under Tr=40%. The average running time (s) per frame is reported.**

Methods	Category	B3				B4				B5				B6				Avg Time
		$IoU$	$F_1$	$P_d$	$F_a \downarrow$	$IoU$	$F_1$	$P_d$	$F_a \downarrow$	$IoU$	$F_1$	$P_d$	$F_a \downarrow$	$IoU$	$F_1$	$P_d$	$F_a \downarrow$	
NOLC [48]	single-Opti	41.43	56.11	87.00	1.23	24.09	38.83	71.33	2.06	56.45	72.16	67.00	0.63	26.22	41.55	48.08	0.46	0.692
NRAM [42]	single-Opti	18.28	30.90	84.00	0.18	21.56	35.48	44.42	0.85	62.03	76.57	69.00	0.37	16.09	27.72	29.58	0.14	1.214
NTFRA [17]	single-Opti	0.01	0.03	6.00	94.00	23.16	37.61	71.25	1.10	3.38	6.55	7.00	0.89	54.46	70.52	51.70	0.08	1.430
PSTNN [43]	single-Opti	18.61	31.38	75.00	0.75	0.06	0.12	0.72	130.1	1.31	2.59	7.00	30.02	3.40	6.57	32.08	0.23	0.380
SRWS [47]	single-Opti	32.14	48.64	90.00	0.96	39.20	56.32	73.17	0.74	51.97	68.40	64.00	0.72	29.05	45.02	50.90	0.17	0.814
ASTTV [23]	multi-Opti	0.09	0.18	69.00	199.5	0.06	0.13	61.42	800.5	29.78	45.89	50.00	0.03	46.01	63.02	51.00	0.49	1.816
IMNN [25]	multi-Opti	75.43	86.00	94.00	0.35	52.98	69.26	89.58	5.75	49.14	61.39	61.00	8.27	53.53	70.84	50.30	0.29	2.273
MFSTPT [13]	multi-Opti	29.84	45.97	77.00	0.47	13.96	24.49	67.67	5.26	63.49	77.67	73.00	0.14	13.27	23.42	51.92	3.46	16.94
NFTDGSTV [22]	multi-Opti	69.33	81.89	98.00	0.21	41.56	58.72	90.17	0.82	62.78	77.14	76.00	0.13	48.48	65.30	51.90	0.15	1.821
TCTV [21]	multi-Opti	32.06	48.55	94.00	1.94	48.44	65.27	90.50	0.87	53.57	69.77	69.00	0.11	51.47	67.96	53.80	0.22	2.372
CTSTC [26]	multi-Opti	60.39	75.30	98.00	0.27	34.21	50.98	64.92	5.46	66.29	79.73	85.00	0.08	52.88	68.21	54.60	0.03	0.145
ACM [7]	single-DL	34.22	50.99	100.0	0.00	2.32	4.53	22.00	33.20	32.58	49.15	90.00	5.42	32.63	49.20	52.50	0.34	0.109
ALCNet [8]	single-DL	32.54	49.11	93.00	1.51	0.05	0.10	0.00	4.24	26.29	41.63	83.00	1.37	27.13	42.68	35.67	2.34	0.086
PBT [41]	single-DL	35.06	51.92	100.0	0.00	0.03	0.06	23.33	89.29	50.75	67.33	96.00	0.18	0.05	0.11	49.50	52.99	0.123
RDIAN [32]	single-DL	1.06	2.10	10.00	2.47	0.00	0.00	0.00	2.91	26.24	41.57	57.00	2.01	1.00	1.98	4.25	3.59	0.076
RPCANet [36]	single-DL	0.43	0.86	5.00	4.38	0.49	0.97	3.75	2.87	22.37	36.56	81.00	2.35	5.73	10.84	31.67	1.91	0.105
NeurSTT [35]	multi-DL	82.48	90.40	100.0	0.13	54.67	70.69	81.17	0.60	82.17	90.21	100.0	0.02	55.88	71.69	52.50	0.46	0.581
optNL-INR	multi-DL	<b>87.47</b>	<b>93.32</b>	<b>100.0</b>	<b>0.09</b>	<b>78.43</b>	<b>87.91</b>	<b>91.42</b>	<b>0.26</b>	<b>81.69</b>	<b>89.92</b>	<b>100.0</b>	<b>0.01</b>	<b>58.54</b>	<b>73.85</b>	<b>55.50</b>	<b>0.00</b>	<b>0.597</b>

vary  $S$  in  $\{1, 3, 5, 8, 10\}$ . To achieve optimal performance, we set the patch size to  $S = 6$ .

**Poly  $\sigma$ :** It governs the local gradient weight distribution in optical flow computation. A larger value results in smoother gradient information and stronger noise suppression, but may lead to details loss. A smaller value makes the gradient changes more sensitive but also increases sensitivity to noise. We vary  $\sigma$  in  $\{0.4, 0.6, 0.8, 1.0, 1.2\}$ . To achieve optimal performance, we set  $\sigma$  to 0.8.

### 5.3 Comparison to State-of-the-art Methods

We compare the proposed optNL-INR with SOTA methods to demonstrate its advantages: The model-based methods include single-frame methods NOLC[48], NRAM[42], NTFRA[17], PSTNN[43], SRWS[47], and multi-frame methods ASTTV-NTLA[23], IMNN-LWEC [25], MFSTPT [13], NFTDGSTV [22], TCTV [21], CTSTC

[26]. The DL-based methods include single-frame methods ACM[7], ALCNet[8], PBT[41], RDIAN[32], RPCANet[36] and multi-frame method NeurSTT[35]. We follow the hyperparameters in the source code and fine-tune them for optimal results.

**5.3.1 Visual Results.** Visual results are shown in Figure 3, with representative results from five typical scenes (datasets A1-A3 and B1-B2). It can be observed that several methods perform poorly on sequences, frequently resulting in target loss across frames. For example, PSTNN fails to detect targets in A3, B1, and B2; MFSTPT and RDIAN also exhibit target loss in A3. Additionally, some methods struggle with background noise suppression. For instance, MFSTPT produces predictions with significant background clutter in A1, A3, and B2, while CTSTC, RDIAN, and NeurSTT undergo weak noise suppression in A3. In contrast, our method demonstrates superior

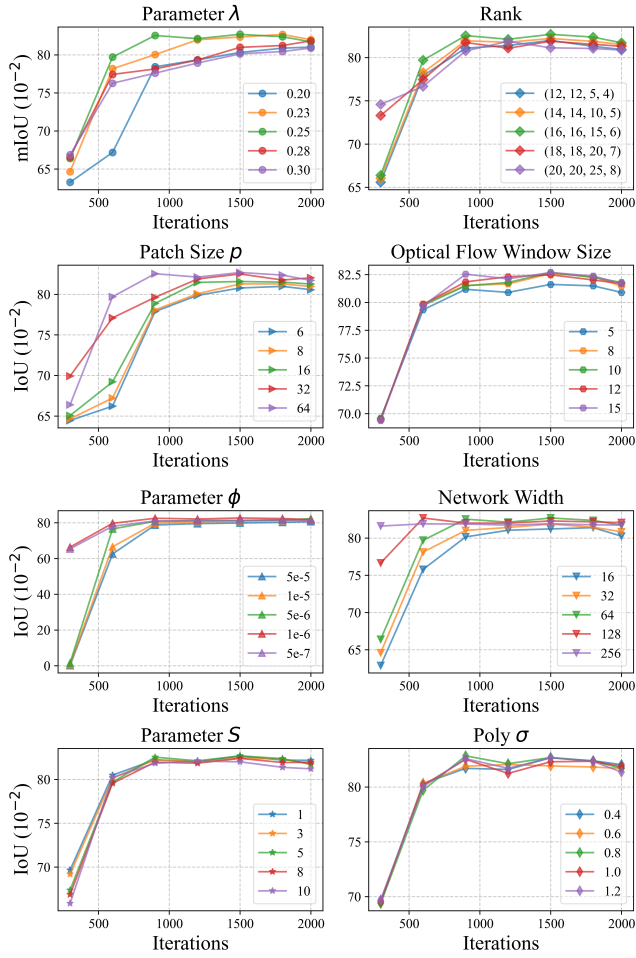


Figure 4: Curves of IoU for different hyperparameters of optNL-INR.

performance in both target detection accuracy and noise suppression capacity. More importantly, it provides more accurate shape predictions of the targets. For example, in B1, MFSTPT yields a fragmented target shape, while the predictions from CTSTC and RDIAN still deviate from the actual target contours. Although NeurSTT performs well, our approach captures finer target details, as seen in A3, where the predicted target shape is more precise. The detailed parameter settings of different comparison methods are provided in Table 1.

**5.3.2 Quantitative Results.** We conducted performance experiments on the ATR and Anti-UAV datasets, comprising 12 scene sequences (A1-A6, B1-B6). The quantitative results are shown in Tables 2, 3, and 4, with average runtime in the last column. In all tables, the best results are **bolded**, and the second-best are underlined.

As observed, multi-frame optimization methods generally outperform single-frame ones, highlighting the effectiveness of temporal information in enhancing detection performance. Single-frame deep methods show limited performance, performing well in specific scenes (e.g., A2, B3) but struggling in others, with  $IoU$  and

$F_1$  scores dropping below 20 in A3, A5, and B4. This suggests that limited sample diversity in sequential images hinders feature learning, even for supervised methods. In contrast, the multi-frame deep method NeurSTT yields impressive results in several scenes, but our method consistently delivers superior and more robust results. Moreover, our method achieves the best results in 11 scenes for  $IoU$  and  $F_1$ , with  $IoU$  reaching 83.81, 83.17, and 87.47 in A2, A4, and B3, and significant improvements in A3, B1, and B4, outperforming the second-best by 31.62, 16.80, and 23.76. Although it ranks second in B5,  $IoU$  and  $F_1$  are only 0.48 and 0.29 lower than the best. For  $P_d$  and  $F_a$ , our method also leads in 11 scenes, with  $P_d$  reaching 100 in A4, B2, B3, and B5, and  $F_a$  reaches 0 in B6 and 0.02 in A2, A3, and A6. Overall, the proposed unsupervised optNL-INR demonstrates strong robustness by enhancing detection accuracy and suppressing noise effectively. Furthermore, while deep learning methods offer faster inference via pre-trained models, our method still remains competitive, processing at around 0.6s per frame compared to other optimization-based baselines.

**5.3.3 Ablation Studies.** We conduct ablation experiments on two main modules: non-local similarity computation and optical flow estimation. The results in Table 5 show a notable improvement in pixel-level metrics between Setting 1 and Setting 2, with  $IoU$  increasing from 71.40 to 75.30 and  $F_1$  rising from 82.98 to 85.45. This indicates that the non-local similarity computation improves background consistency and suppresses noise, improving the saliency of small targets. Comparing Setting 2 and Setting 3, the target-level metric  $P_d$  increases from 90.75 to 94.25, demonstrating that the optical flow module effectively mitigates moving target loss. Notably, the false alarm rate  $F_a$  remains low across all settings, demonstrating the robustness of optNL-INR in background suppression.

Table 5: Component ablation results in average values of  $IoU$  ( $10^{-2}$ ),  $F_1$  ( $10^{-2}$ ),  $P_d$  ( $10^{-2}$ ) and  $F_a$  ( $10^{-5}$ )

Settings	Modules		Average Metrics			
	Nonlocal	Optical	$IoU$	$F_1$	$P_d$	$F_a \downarrow$
1	×	×	71.41	82.98	88.50	<u>0.53</u>
2	✓	×	<u>75.30</u>	85.45	90.75	<u>0.59</u>
3	✓	✓	<b>77.53</b>	<b>87.15</b>	<b>94.25</b>	<b>0.29</b>

## 5.4 Conclusion

We propose a novel motion-enhanced non-local similarity implicit neural representation model, termed optNL-INR, for infrared dynamic background estimation and small moving targets detection. By calculating optical flow across consecutive frames, the model captures motion-significant small targets and employs a multi-frame fusion strategy to improve the robustness of motion saliency estimation. Subsequently, non-local similarity patch tensors of low-rank background are constructed to capture background consistency information, thereby improving the capability of dynamic background estimation. Finally, non-linear estimation of these tensors is performed within a continuous domain using low-rank constrained INRs, achieving more accurate target-background separation. Comparative experiments against 17 baselines demonstrate the effectiveness and robustness of our method.

## References

- [1] Xiangzhi Bai and Yanguang Bi. 2018. Derivative entropy-based contrast measure for infrared small-target detection. *IEEE Transactions on Geoscience and Remote Sensing* 56, 4 (2018), 2452–2466.
- [2] Yuanning Bai, Ruimin Li, Shuiping Gou, Chenchen Zhang, Yaohong Chen, and Zhihui Zheng. 2022. Cross-connected bidirectional pyramid network for infrared small-dim target detection. *IEEE Geoscience and Remote Sensing Letters* 19 (2022), 1–5.
- [3] Stanley H. Chan, Xiran Wang, and Omar A. Elgendy. 2017. Plug-and-Play ADMM for Image Restoration: Fixed-Point Convergence and Applications. *IEEE Transactions on Computational Imaging* 3, 1 (2017), 84–98.
- [4] CL Philip Chen, Hong Li, Yantao Wei, Tian Xia, and Yuan Yan Tang. 2013. A local contrast method for small infrared target detection. *IEEE transactions on geoscience and remote sensing* 52, 1 (2013), 574–581.
- [5] Shengjia Chen, Luping Ji, Sicheng Zhu, Mao Ye, Haohao Ren, and Yongsheng Sang. 2024. Towards dense moving infrared small target detection: New datasets and baseline. *IEEE Transactions on Geoscience and Remote Sensing* (2024).
- [6] Yimian Dai and Yiquan Wu. 2017. Reweighted infrared patch-tensor model with both nonlocal and local priors for small target detection. *IEEE journal of selected topics in applied earth observations and remote sensing* 10, 8 (2017), 3752–3767.
- [7] Yimian Dai, Yiquan Wu, Fei Zhou, and Kobus Barnard. 2021. Asymmetric contextual modulation for infrared small target detection. In *Proceedings of the IEEE/CVF winter conference on applications of computer vision*. 950–959.
- [8] Yimian Dai, Yiquan Wu, Fei Zhou, and Kobus Barnard. 2021. Attentional local contrast networks for infrared small target detection. *IEEE transactions on geoscience and remote sensing* 59, 11 (2021), 9813–9824.
- [9] Suyog D Deshpande, Meng Hwa Er, Ronda Venkateswarlu, and Philip Chan. 1999. Max-mean and max-median filters for detection of small targets. In *Signal and Data Processing of Small Targets 1999*, Vol. 3809. SPIE, 74–83.
- [10] David L Donoho. 2002. De-noising by soft-thresholding. *IEEE transactions on information theory* 41, 3 (2002), 613–627.
- [11] Gunnar Farnelbäck. 2003. Two-frame motion estimation based on polynomial expansion. In *Image Analysis: 13th Scandinavian Conference, SCIA 2003 Halmstad, Sweden, June 29–July 2, 2003 Proceedings* 13. Springer, 363–370.
- [12] Chenqiang Gao, Deyu Meng, Yi Yang, Yongtao Wang, Xiaofang Zhou, and Alexander G Hauptmann. 2013. Infrared patch-image model for small target detection in a single image. *IEEE transactions on image processing* 22, 12 (2013), 4996–5009.
- [13] Yuxin Hu, Yapeng Ma, Zongxu Pan, and Yuhua Liu. 2022. Infrared dim and small target detection from complex scenes via multi-frame spatial-temporal patch-tensor model. *Remote Sensing* 14, 9 (2022), 2234.
- [14] Yuanxin Huang, Xiyang Zhi, Jianming Hu, Lijian Yu, Qichao Han, Wenbin Chen, and Wei Zhang. 2024. LMAFormer: Local Motion Aware Transformer for Small Moving Infrared Target Detection. *IEEE Transactions on Geoscience and Remote Sensing* (2024).
- [15] Kingma. 2015. ADAM: A Method for Stochastic Optimization. In *International Conference on Learning Representations*.
- [16] Tamara G Kolda and Brett W Bader. 2009. Tensor decompositions and applications. *SIAM Rev* 51, 3 (2009), 455–500.
- [17] Xuan Kong, Chunping Yang, Siying Cao, Chaohai Li, and Zhenming Peng. 2021. Infrared small target detection via nonconvex tensor fibered rank approximation. *IEEE Transactions on Geoscience and Remote Sensing* 60 (2021), 1–21.
- [18] Boyang Li, Chao Xiao, Longguang Wang, Yingqian Wang, Zaiping Lin, Miao Li, Wei An, and Yulan Guo. 2022. Dense nested attention network for infrared small target detection. *IEEE Transactions on Image Processing* 32 (2022), 1745–1758.
- [19] Ruoqing Li, Wei An, Chao Xiao, Boyang Li, Yingqian Wang, Miao Li, and Yulan Guo. 2023. Direction-coded temporal U-shape module for multiframe infrared small target detection. *IEEE Transactions on Neural Networks and Learning Systems* (2023).
- [20] Fanzhao Lin, Kexin Bao, Yong Li, Dan Zeng, and Shiming Ge. 2024. Learning contrast-enhanced shape-biased representations for infrared small target detection. *IEEE Transactions on Image Processing* (2024).
- [21] Pei Liu, Jiangjun Peng, Hailin Wang, Danfeng Hong, and Xiangyong Cao. 2024. Infrared Small Target Detection via Joint Low Rankness and Local Smoothness Prior. *IEEE Transactions on Geoscience and Remote Sensing* (2024).
- [22] Ting Liu, Jungang Yang, Boyang Li, Yingqian Wang, and Wei An. 2023. Infrared small target detection via nonconvex tensor Tucker decomposition with factor prior. *IEEE Transactions on Geoscience and Remote Sensing* 61 (2023), 1–17.
- [23] Ting Liu, Jungang Yang, Boyang Li, Chao Xiao, Yang Sun, Yingqian Wang, and Wei An. 2021. Nonconvex tensor low-rank approximation for infrared small target detection. *IEEE Transactions on Geoscience and Remote Sensing* 60 (2021), 1–18.
- [24] Ziling Lu, Zhenghua Huang, Qiong Song, Hongyin Ni, and Kun Bai. 2023. Infrared small target detection based on joint local contrast measures. *Optik* 273 (2023), 170437.
- [25] Yuan Luo, Xiaorun Li, Shuhan Chen, Chaoqun Xia, and Liaoying Zhao. 2022. IMNN-LWEC: A novel infrared small target detection based on spatial-temporal tensor model. *IEEE Transactions on Geoscience and Remote Sensing* 60 (2022), 1–22.
- [26] Yuan Luo, Xiaorun Li, Jing Wang, and Shuhan Chen. 2024. Clustering and tracking-guided infrared spatial-temporal small target detection. *IEEE Transactions on Geoscience and Remote Sensing* (2024).
- [27] Yisi Luo, Xile Zhao, Zhemin Li, Michael K Ng, and Deyu Meng. 2023. Low-rank tensor function representation for multi-dimensional data recovery. *IEEE transactions on pattern analysis and machine intelligence* 46, 5 (2023), 3351–3369.
- [28] Yisi Luo, Xile Zhao, Zhemin Li, Michael K. Ng, and Deyu Meng. 2024. Low-Rank Tensor Function Representation for Multi-Dimensional Data Recovery. *IEEE Transactions on Pattern Analysis and Machine Intelligence* 46, 5 (2024), 3351–3369.
- [29] Ben Mildenhall, Pratul P Srinivasan, Matthew Tancik, Jonathan T Barron, Ravi Ramamoorthi, and Ren Ng. 2021. NeRF: Representing scenes as neural radiance fields for view synthesis. *Commun. ACM* 65, 1 (2021), 99–106.
- [30] Jean-Francois Rivest and Roger Fortin. 1996. Detection of dim targets in digital infrared imagery by morphological image processing. *Optical Engineering* 35, 7 (1996), 1886–1893.
- [31] Vincent Sitzmann, Julien Martel, Alexander Bergman, David Lindell, and Gordon Wetzstein. 2020. Implicit Neural Representations with Periodic Activation Functions. *Advances in Neural Information Processing Systems* 33 (2020), 7462–7473.
- [32] Heng Sun, Junxiang Bai, Fan Yang, and Xiangzhi Bai. 2023. Receptive-field and direction induced attention network for infrared dim small target detection with a large-scale dataset IRDST. *IEEE Transactions on Geoscience and Remote Sensing* 61 (2023), 1–13.
- [33] Yang Sun, Jungang Yang, and Wei An. 2020. Infrared dim and small target detection via multiple subspace learning and spatial-temporal patch-tensor model. *IEEE Transactions on Geoscience and Remote Sensing* 59, 5 (2020), 3737–3752.
- [34] Guanghui Wang, Bingjie Tao, Xuan Kong, and Zhenming Peng. 2021. Infrared small target detection using nonoverlapping patch spatial-temporal tensor factorization with capped nuclear norm regularization. *IEEE Transactions on Geoscience and Remote Sensing* 60 (2021), 1–17.
- [35] Fengyi Wu, Simin Liu, Haoan Wang, Bingjie Tao, Junhai Luo, and Zhenming Peng. 2024. Neural Spatial-Temporal Tensor Representation for Infrared Small Target Detection. *arXiv preprint arXiv:2412.17302* (2024).
- [36] Fengyi Wu, Tianfang Zhang, Lei Li, Yian Huang, and Zhenming Peng. 2024. RPCANet: Deep unfolding RPCA based infrared small target detection. In *Proceedings of the IEEE/CVF Winter Conference on Applications of Computer Vision*. 4809–4818.
- [37] Peng Wu, Honghe Huang, Hanxiang Qian, Shaojing Su, Bei Sun, and Zhen Zuo. 2022. SRCANet: Stacked residual coordinate attention network for infrared ship detection. *IEEE Transactions on Geoscience and Remote Sensing* 60 (2022), 1–14.
- [38] Xin Wu, Danfeng Hong, and Jocelyn Chaussoot. 2022. UIU-Net: U-Net in U-Net for infrared small object detection. *IEEE Transactions on Image Processing* 32 (2022), 364–376.
- [39] Puti Yan, Runze Hou, Xuguang Duan, Chengfei Yue, Xin Wang, and Xibin Cao. 2023. STDMA-Net: Spatio-temporal differential multiscale attention network for small moving infrared target detection. *IEEE transactions on geoscience and remote sensing* 61 (2023), 1–16.
- [40] Hai Yang, Jing Liu, Zhe Wang, Zhiling Fu, Qinyan Tan, and Saisai Niu. 2024. MAPFF: Multi-Angle Pyramid Feature Fusion Network for Infrared Dim Small Target Detection. *IEEE Transactions on Geoscience and Remote Sensing* (2024).
- [41] Huoren Yang, Tingkui Mu, Ziyue Dong, Zicheng Zhang, Bin Wang, Wei Ke, Qiujie Yang, and Zhiping He. 2024. Pbt: Progressive background-aware transformer for infrared small target detection. *IEEE Transactions on Geoscience and Remote Sensing* (2024).
- [42] Landan Zhang, Lingbing Peng, Tianfang Zhang, Siying Cao, and Zhenming Peng. 2018. Infrared small target detection via non-convex rank approximation minimization joint  $l_2, 1$  norm. *Remote Sensing* 10, 11 (2018), 1821.
- [43] Landan Zhang and Zhenming Peng. 2019. Infrared small target detection based on partial sum of the tensor nuclear norm. *Remote Sensing* 11, 4 (2019), 382.
- [44] Mingjin Zhang, Bate Li, Tianyu Wang, Haichen Bai, Ke Yue, and Yunsong Li. 2023. Chfnct: Curvature half-level fusion network for single-frame infrared small target detection. *Remote Sensing* 15, 6 (2023), 1573.
- [45] Mingjin Zhang, Ke Yue, Jing Zhang, Yunsong Li, and Xinbo Gao. 2022. Exploring feature compensation and cross-level correlation for infrared small target detection. In *Proceedings of the 30th ACM International Conference on Multimedia*. 1857–1865.
- [46] Tianfang Zhang, Lei Li, Siying Cao, Tian Pu, and Zhenming Peng. 2023. Attention-guided pyramid context networks for detecting infrared small target under complex background. *IEEE Trans. Aerospace Electron. Systems* 59, 4 (2023), 4250–4261.
- [47] Tianfang Zhang, Zhenming Peng, Hao Wu, Yanmin He, Chaohai Li, and Chunping Yang. 2021. Infrared small target detection via self-regularized weighted sparse model. *Neurocomputing* 420 (2021), 124–148.
- [48] Tianfang Zhang, Hao Wu, Yuhua Liu, Lingbing Peng, Chunping Yang, and Zhenming Peng. 2019. Infrared small target detection based on non-convex optimization with  $L_p$ -norm constraint. *Remote Sensing* 11, 5 (2019), 559.
- [49] Zhiyuan Zhang, Pan Gao, Sixiang Ji, Xun Wang, and Ping Zhang. 2023. Infrared small target detection combining deep spatial-temporal prior with traditional

priors. *IEEE Transactions on Geoscience and Remote Sensing* 61 (2023), 1–18.  
[50] Yuhan Zhong, Zhiguang Shi, Yan Zhang, Yong Zhang, and Hanyu Li. 2024. CSAN-UNet: Channel Spatial Attention Nested UNet for Infrared Small Target Detection.

*Remote Sensing* 16, 11 (2024), 1894.